CrystEngComm

Accepted Manuscript

ROYAL SOCIETY OF CHEMISTRY

www.rsc.org/crystengcomm

Cite this: DOI: 10.1039/c0xx00000x

www.rsc.org/xxxxxx

ARTICLE TYPE

The electrochemical properties, nitrogen adsorption and photocatalytic activities of three 3D metal–organic frameworks bearing the rigid terphenyl tetracarboxylates ligands

Bao Mu, Chang-xia Li, Ming Song, Yan-li Ren, Ru-Dan Huang*

Key Laboratory of Cluster Science of Ministry of Education, School of Chemistry, Beijing Institute of Technology, Beijing, 100081, P. R. China

Received (in XXX, XXX) Xth XXXXXXXXX 200X, Accepted Xth XXXXXXXXX 200X
DOI: 10.1039/b000000x

Three new three-dimensional (3D) metal–organic frameworks (MOFs) derived from terphenyl tetracarboxylates, namely, $[Mn(\mathbf{H_2L})]_n$ (**1**), $\{[Ni_3(\mathbf{L})(\mu_3\text{-}OH)_2(H_2O)_4]_2\cdot 3H_2O\}_n$ (**2**) and $\{[(CH_3)_2NH_2]_2[Zn(\mathbf{L})]\cdot 2DMF\}_n$ (**3**) ($\mathbf{H_4L}$ = [1,1′:4′,1″-terphenyl]-2′,4,4″,5′-tetracarboxylic acid), have been synthesized and characterized by elemental analyses, IR spectra, thermogravimetric (TG) analyses, powder X-ray diffraction (PXRD) and single-crystal X-ray diffraction. Complex **1** represents a 6-connected $\{4^{12}\cdot 6^3\}$ framework, which contains 1D stair-type chain and 2D layer. Complex **2** displays the complicated $\{4^{11}\cdot 6^{12}\cdot 8^5\}\{4^2\cdot 6\}\{4^3\cdot 6^3\}\{4^3\}\{4^4\cdot 6^2\}\{4^8\cdot 6^6\cdot 8\}$ topology, in which Ni-O chains play an important role in the whole framework. In complex **3**, the wave-like and "H"-like 1D chains link each other to create the 3D architecture with $\{4^2\cdot 8^4\}$ topology. The introduction of the different metal ions and the diversities synthesis processes lead to the great differences of the final 3D frameworks. In addition, the fluorescence properties reveal that complex **3** containing Zn^{II} possesses the fluorescent intensity, and complexes **1**–**2** based on Mn^{II} and Ni^{II} have no florescent activity. The electrochemical properties exhibit that complex **2** possesses electrocatalytic activity to the reduction of nitrite. Photocatalytic properties indicate that complex **1** has good catalytic activity for the degradation of methylene blue (MB). The nitrogen adsorption reveals that complex **3** has adsorption property for nitrogen at 77 K.

Introduction

In the last two decades, metal–organic frameworks (MOFs) has become the focus of concern for the chemists ascribing not only the absorbing architectures and intricate topologies but also the extensive applications in gas adsorption/separation, electrochemistry, fluorescence, magnetic properties, catalysis and so on [1-2]. In the field of photocatalysis, utilizing conventional semiconductor metal oxides to degrade the organic dyes with the chromophore azo group (–N=N–) is not the only solution. The researches of photocatalytic materials based on MOFs become gradually an increasingly promising area in virtue of good photocatalytic efficiency from plenty of MOFs [3]. In the MOFs pholocatalysts, the differences of interactions from both inorganic and organic moieties may lead to the diversities from metal−organic ligand charge transfer [4]. Furthermore, the MOFs possessing the specific structures may exhibit better photocatalytic activities. In view of the above features, to our knowledge, some groups have explored the photocatalytic performance of MOFs deeply [5]. Li *et al.* synthesized a MOF constructed by 3D anionic framework and 1D cationic chains, which reveals the good degraded effect for methyl orange (MO) [6a]. Hou *et al.* studied the influences of a series of MOFs containing polynuclears on photocatalytic degradation of the organic dyes, showing that the title complexes have high photocatalytic activities in methylene blue (MB)/MO degradation owing to different kinds of nuclei from the cluster complexes [6b]. Therefore, the photocatalytic activities of MOFs with the various constructions should be needed to explore further.

The emergence of good performances has great relevance to the formation of different structures from MOFs [7]. The selection of the organic ligands is one of the most significant factors to build the targetable MOFs [8]. The O-donor polycarboxylates ligands, as the commonest organic ligands, have been used to construct a number of MOFs possessing both the attractive architectures and outstanding properties [9]. The development of the polycarboxylates

Key Laboratory of Cluster Science of Ministry of Education, School of Chemistry, Beijing Institute of Technology, Beijing, 100081, P. R. China; Email: huangrd@bit.edu.cn

†Electronic Supplementary Information (ESI) available: IR, TG and additional figures. CCDC: 1436966–1436968. For ESI and crystallographic data in CIF or other electronic format see DOI: 10.1039/b000000x.

is from the simple aromatic dicarboxylates to many different types of aromatic polycarboxylates, such as tripodal tricarboxylates ligands, branch-shape tetracarboxylates ligands, which play an important role in generating the diverse MOFs exhibiting the remarkable properties [10]. In this respect, Yaghi's group has obtained hundreds of polycarboxylates-based MOFs including MOF-5. They recently introduced the tripodal ligands 4,4′,4″-benzene-1,3,5-tryil-tribenzoic acids into the aluminum system to synthesize two new MOFs (MOF-519 and MOF-520) in the different conditions, and the materials have high methane storage capacity. It is worth mentioning that MOF-519 shows the extraordinary working capacity [11a]. In addition, the other research groups also apply themselves to polycarboxylates-based MOFs. For example, Ma and his co-workers chose resorcin[4]arene-based tetracarboxylate and d^{10} metal Cd^{II} ions as the reactants to get the functional MOFs. Those complexes were carried out metal-ion exchange with Co^{II} ions, and they have selectivity for the adsorption of organic dyes [11b]. Thus it can be seen that MOFs constructed by the polycarboxylates have the extensively developmental prospects in many fileds.

Taking these into account, in this work, the rigid terphenyl tetracarboxylate is selected as the organic ligands because not only the presence of rigid terphenyl moieties benefits the formation of pore frameworks but also this ligand has the ability of producing the ·OH active species to cause the photocatalytic activities for degradation some organic dyes. In view of this rigid terphenyl tetracarboxylate ligand, three 3D MOFs, formulas, $[Mn(\mathbf{H_2L})]_n$ (**1**), $\{[Ni_3(\mathbf{L})(\mu_3\text{-}OH)_2(H_2O)_4]_2\cdot 3H_2O\}_n$ (**2**) and $\{[(CH_3)_2NH_2]_2[Zn(\mathbf{L})]\cdot 2DMF\}_n$ (**3**) ($\mathbf{H_4L}$ = [1,1′:4′,1″-terphenyl]-2′,4,4″,5′-tetracarboxylic acid), were obtained. The fluorescence properties of the title complexes as well as the electrochemical behavior of complex **2** have been investigated. Moreover, the photocatalytic properties show that complexes **1**–**3** exhibit different degradative effects for MB. The nitrogen adsorption for complexes **2**–**3** has been researched at 77 K.

Experimental section

Materials and characterization

All the chemicals were from the commercial sources, and they were without further purification. The elemental analyses (C, H, and N) were measured on a Perkin-Elmer 2400 CHN elemental analyzer. The FT-IR spectra (KBr pellets) were collected using a Nicolet 170SX spectrometer. The powder X-ray diffraction (PXRD) were carried out on a Siemens D5005 diffractometer (Cu Ka radiation, λ = 1.5410 Å). Thermogravimetric (TG) analyses of complexes **1**–**3** were measured on a Exstar SII TG/DTA 7200 thermal analyzer. Fluorescence spectra were recorded on a Hitachi F-4600 fluorescence/phosphorescence spectrophotometer. UV-Vis absorption spectra were taken on a TU-1901 UV-vis spectrophotometer. Nitrogen adsorption experiments were carried out on a TriStarII3020 (Micromeritics Instrument Corporation) apparatus at 77 K. Electrochemical measurements were performed on a CHI 660E Electrochemical Quartz Crystal Microbalance. The platinum wire, Ag/AgCl and complex **2** bulk-modified carbon paste electrode (**2**–CPE) was used as the auxiliary electrode, reference electrode and working electrode, respectively.

Table 1. Crystal data and structure refinements for complexes **1**–**3**

Complex	**1**	**2**	**3**
Formula	$C_{22}H_{12}MnO_8$	$C_{44}H_{46}Ni_6O_{31}$	$C_{32}H_{40}ZnN_4O_{10}$
Formula wt.	459.26	1422.95	706.05
Cryst. syst	Triclinic	Triclinic	Monoclinic
Space group	*P-1*	*P-1*	*C2/c*
a (Å)	4.8040(3)	11.0031(9)	23.432(2)
b (Å)	9.8809(7)	11.2217(11)	9.5422(8)
c (Å)	10.0661(9)	11.6959(11)	18.9958(17)
α (°)	75.987(1)	69.193(1)	90
β (°)	81.807(2)	79.676(1)	125.964(2)
γ (°)	79.391(1)	81.008(2)	90
V (Å ^{3})	453.26(6)	1321.3(2)	3437.7(5)
Z	1	1	4
D_{calc} (g/cm^3)	1.682	1.788	1.364
μ/mm^{-1}	0.781	3.176	0.775
F(000)	233	726	1480
R_{int}	0.047	0.114	0.051
$R_1{}^a$ [$I>2\sigma(I)$]	0.0702	0.0947	0.0448
$wR_2{}^b$(all data)	0.1891	0.2865	0.1147
GOF	1.005	1.034	1.009
$\Delta\rho_{max}$(e Å^{-3})	0.948	1.178	0.488
$\Delta\rho_{min}$(e Å^{-3})	–0.905	–1.452	–0.673

$^a R_1 = \Sigma(||F_o| - |F_c||)/\Sigma|F_o|$ $^b wR_2 = [\Sigma w(|F_o|^2 - |F_c|^2)^2/(\Sigma w|F_o|^2)^2]^{1/2}$

Preparation of the title complexes

Synthesis of $[Mn(H_2L)]_n$ (1). The mixture of $MnCl_2\cdot 4H_2O$ (0.0396 g, 0.20 mmol), $\mathbf{H_4L}$ (0.0406 g, 0.10 mmol) and H_2O (10 mL) was put in a 25 mL Teflon reactor, keeping at 150°C for 3 days. When the Teflon reactor was cooled to room temperature, the yellow block crystals were collected. Yield 28% based on Mn. Anal. Calc. for $C_{22}H_{12}MnO_8$ (459.26): C, 57.53; H, 2.63%. Found: C, 57.49; H, 2.65%. IR (KBr, cm^{-1}): 3150 (s), 1660 (s), 1565 (s), 1495 (m), 1407 (s), 1272 (s), 1175 (m), 1144 (m), 1098 (w), 1014 (m), 921 (m), 885 (m), 831 (m), 799 (m), 779 (m), 720 (m), 628 (w), 542 (w), 501 (w).

Synthesis of $\{[Ni_3(L)(\mu_3\text{-}OH)_2(H_2O)_4]_2\cdot 3H_2O\}_n$ (2). The mixture of $Ni(NO_3)_2\cdot 6H_2O$ (0.1746 g, 0.60 mmol), $\mathbf{H_4L}$ (0.0203 g, 0.05 mmol), 1 mol·L^{-1} HCl aqueous solution (0.07 mL) and H_2O (10 mL) was placed in a 25 mL Teflon reaction kettle, and it was heated at 160°C for 3 days. The green crystals were obtained. Yield 19% based on Ni. Anal. Calc. for $C_{44}H_{46}Ni_6O_{31}$ (1422.95): C, 37.14; H, 3.26%. Found: C, 37.12; H, 3.27%. IR (KBr, cm^{-1}): 3585 (w), 3140 (s), 1685 (s), 1639 (s), 1608 (m), 1565 (s), 1399 (s), 1344 (m), 1282 (m), 1257 (m), 1177 (w), 1129 (w), 1067 (w), 1001 (m), 931 (w), 857 (m), 803 (m), 771 (w), 722 (m), 642 (w), 592 (w), 533 (w).

Synthesis of $\{[(CH_3)_2NH_2]_2[Zn(L)]\cdot 2DMF\}_n$ (3). The mixture of $Zn(NO_3)_2\cdot 6H_2O$ (0.0148 g, 0.05 mmol), $\mathbf{H_4L}$ (0.0162 g, 0.04 mmol), 1 mol·L^{-1} HCl aqueous solution (0.15 mL), DMF (3 mL) and H_2O (3 mL) was transfered in a 25 mL Teflon reactor, keeping at 110°C for 5 days. Yield 21% based on Zn. Anal. Calc. for $C_{32}H_{40}ZnN_4O_{10}$ (706.05): C, 54.43; H, 5.71%. Found: C, 54.45; H, 5.69%. IR (KBr, cm^{-1}): 3420 (w), 3132 (s), 1671 (s),

1603 (s), 1474 (m), 1390 (s), 1341 (s), 1259 (m), 1187 (w), 1151 (w), 1094 (m), 1044 (w), 1016 (m), 910 (w), 873 (m), 840 (m), 785 (m), 741 (w), 711 (m), 661 (w), 572 (m), 503 (w).

X-ray crystallographic study

Single-crystal X-ray diffraction data were performed on a Bruker APEX diffractometer with Mo or Cu Kα (graphite monochromator, λ=0.71073 Å for **1** and **3**, λ=1.54178 Å for **2**) at 298 K for **1** and **3**, 293 K for **2**. The structures of complexes **1**–**3** were solved by direct methods and refined by the full-matrix least-squares methods on F^2 with the *SHELXTL* package [12a] and the title complexes were also solved through Olex2 1.2 software [12b-c]. All the non-hydrogen atoms were refined anisotropically, and the hydrogen atoms of the carboxylate ligand were generated theoretically. The O16 of complex **2** was disposed by half-occupied method. The crystal data and structure refinements of the title complexes are summarized in Table 1. Selected bond distances (Å) and angles (°) for complexes **1**–**3** are listed in Tables S1−S3 (Supporting Information). The hydrogen-bonding parameters for the part of complex **3** are summarized in Table S4. The CCDC numbers 1436966–1436968 for complexes **1**−**3** are the supplementary crystallographic data in this paper.

Table 2. Coordination modes of $\mathbf{H_4L}$ ligand in complexes **1**−**3**. Color legend: orange, Mn; green, Ni; yellow, Zn; light gray, C; red, O; charcoal gray, H.

Complex 1	Complex 2	Complex 3
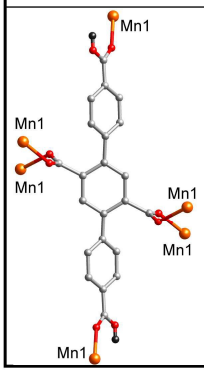	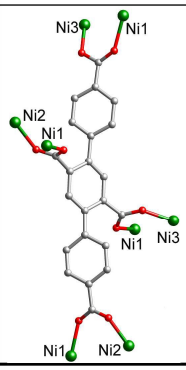	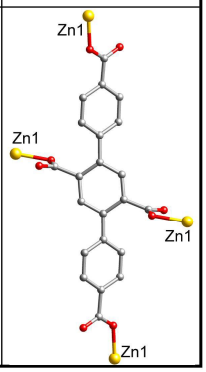

Results and discussion

Description of crystal structures

*[Mn(**H$_2$L**)]$_n$ (1)*

The single-crystal X-ray structural analysis shows that complex **1** belongs to triclinic P-1 space group. Mn1 atom lies on an inversion centre and the asymmetric unit has half of a $\mathbf{H_2L}$ ligand lying about another inversion centre. The metal Mn^{II} ion is lighted by six oxygen atoms (O1, O1#5, O2#3, O2#2, O4#1 and O4#4) from carboxyl groups of six separated $\mathbf{H_2L}$ ligands, possessing a distorted {MnO_6} octahedral sphere with the Mn–O distances of 2.188(3)–2.243(4) Å (Fig. 1). The partially deprotonated $\mathbf{H_2L}$ ligand adopts two kinds of coordination patterns: monodentate and bidentate (Table 2). The carboxyl groups with different coordination modes connect the Mn^{II} ions to create different structures. The monodentate carboxyl oxygen atoms from two-sided parallel phenyl rings are linked by metal Mn^{II} ions, forming stair-type 1D chain with Mn···Mn distance of 19.936 Å (Fig. 2a). While the other bidentate carboxyl oxygen atoms from the central phenyl ring coordinate with Mn^{II} ions to generate a 2D layer which contains the "8"-type Mn-COO^- chains (Fig. 2b). Finally, the 1D stair-type chain and 2D layer link each other to construct the 3D framework (Fig. S1).

The topological analysis reveals that complex **1** exhibits a uninodal 6-connected framework with a Schläfli symbol of $\{4^{12}\cdot6^3\}$, in which both metal Mn^{II} ion and $\mathbf{H_2L}$ ligand are treated as 6-connected nodes, as shown in Fig. 2c.

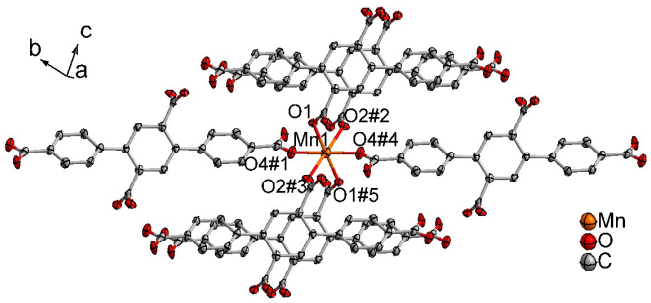

Fig. 1. The coordination environment of the Mn^{II} ion in complex **1** (#1 1 + x, – 1 + y, z; #2 1 + x, y, z; #3 1 – x, – y, 1 – z; #4 1 – x, 1 – y, 1 – z; #5 2 – x, – y, 1 – z).

*{[Ni_3(**L**)(μ_3-OH)$_2$(H_2O)$_4$]$_2$·3H_2O}$_n$ (2)*

The X-ray crystal data exhibits that complex **2** crystallizes triclinic P-1 space group, and it reveals a complicated 3D framework based on the 1D Ni-O chains. The asymmetric unit is composed of six Ni^{II} ions, two fully deprotonated **L** ligands, four μ_3-bridging hydroxyl groups, eight coordinated water molecules and three lattice water molecules. All the Ni^{II} ions are located in a octahedral configuration with different coordination environments (Fig. 3). Ni1 is furnished by four oxygen atoms (O3, O8#2, O10 and O11#3) from carboxyl groups of four separated **L** ligands and two oxygen atoms (O1 and O2) of hydroxyl groups. Ni2 and Ni3 is bonded by two oxygen atoms from carboxyl groups of two separated **L** ligands, two hydroxyl oxygen atoms and two oxygen atoms of the coordinated water molecules.

The Ni–O distances are in the range of 1.9942 to 2.1179 Å. Different from complex **1**, all the carboxylic oxygen atoms from **L** ligand of complex **2** coordinate with Ni^{II} ions (Table 2). In the **L** ligand, there is the dihedral angle of 3.86º between the bilaterally phenyl rings, and the dihedral angles from the bilaterally phenyl rings and the central phenyl ring are 52.67º and 54.07º, respectively. The carboxylic oxygen atoms of bilateral phenyl rings and carboxylic oxygen atoms of the central phenyl ring link the Ni^{II} ions, generating 1D straight chain and "H"-like chain, respectively (Fig. 4a). The μ_8-bridging **L** ligands connect Ni^{II} ions to create a 3D framework containing 1D Ni-O chains, in which $(Ni3)_2$-Ni1-$(Ni2)_2$-Ni1 arrange alternately, displaying the different Ni-Ni units (Fig. 4b). In $(Ni3)_2$-Ni1 unit, the centre Ni3-O quadrangle is edge-shared with the adjacent polygons (Fig. S2). In $(Ni2)_2$-Ni1 unit, the centre Ni2-O rhombus is nested the peripheral polygons (Fig. S3). The hydroxyl groups link three metal Ni^{II} ions, sustaining the whole 3D architecture further (Fig. S4). When lattice water molecules are removed, 13% voids exist in the framework. Moreover, there are O–H···O hydrogen bonding interactions between the oxygen atoms (O2W, O3W and O4W

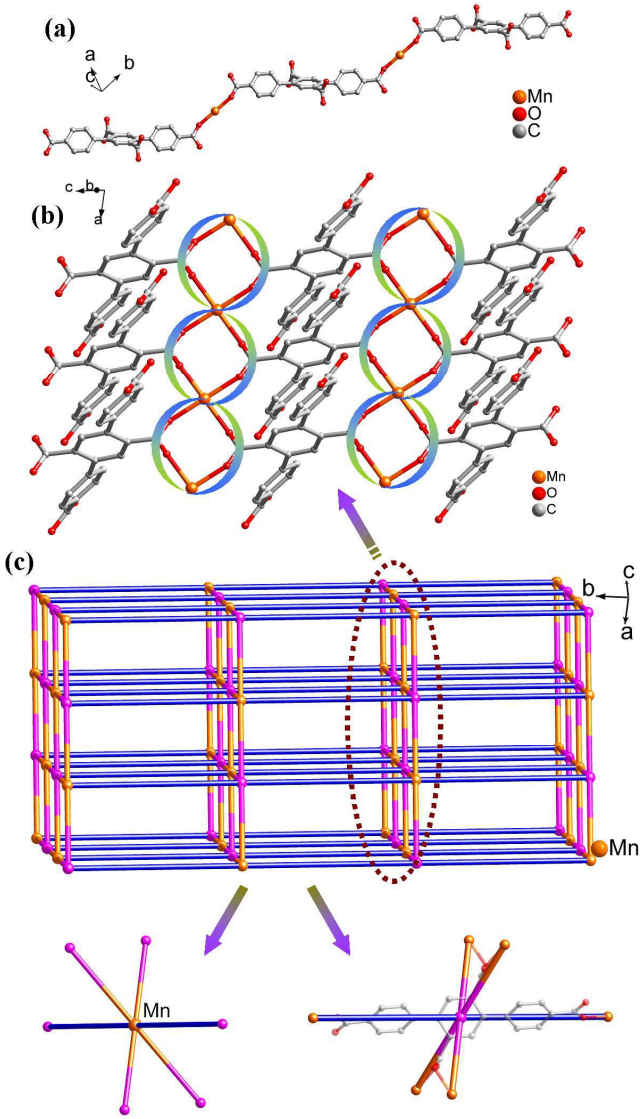

Fig. 2. (a) The 1D stair-type chain composed of monodentate carboxyl oxygen atoms and Mn^{II} ions in complex **1**. (b) The 2D layer composed of bidentate carboxyl oxygen atoms and Mn^{II} ions in complex **1**. (c) The schematic of the 6-connected 3D framework with $\{4^{12}\cdot6^3\}$ topology.

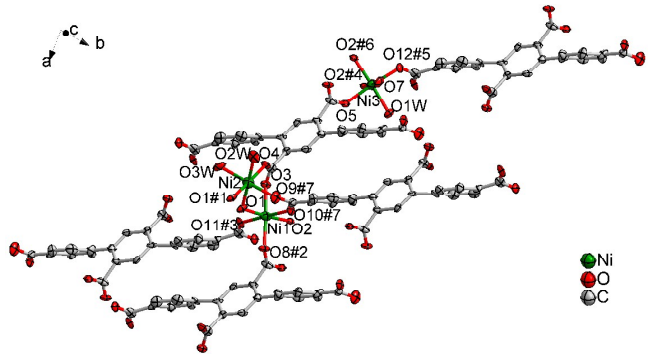

Fig. 3. The coordination environment of the Ni^{II} ion in complex **2** (#1 2–x, –y, 1–z; #2 1+x, y, z; #3 2–x, –y, –z; #4 –1+x, y, z; #5 –1+x, 1+y, z; #6 1–x, 1–y, –z; #7 1–x, 1–y, 1–z).

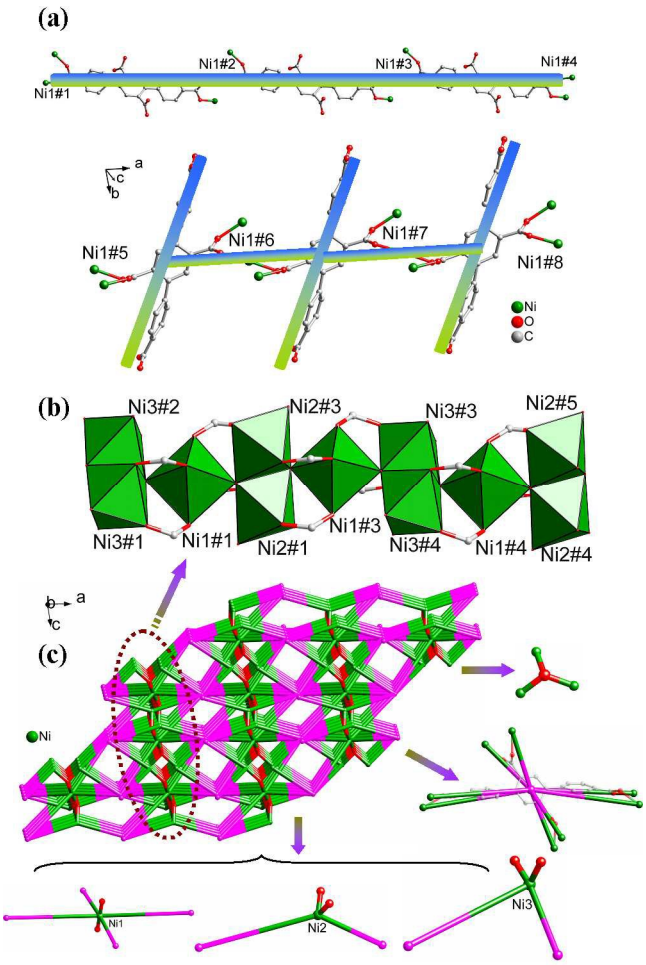

Fig. 4. (a) The 1D straight chain and "H"-like chain composed of the carboxyl oxygen atoms from the different positions (#1 –2–x, 3–y, 3–z; #2 –1–x, 2–y, 2–z; #3 –x, 1–y, 1–z; #4 1–x, –y, –z; #5 –2+x, –1+y, –1+z; #6 –1+x, –1+y, –1+z; #7 x, –1+y, –1+z; #8 1+x, –1+y, –1+z). (b) The 1D Ni-O chains in **2** (#1 1+x, y, –1+z; #2 1–x, 2–y, –z; #3 1–x, 1–y, 1–z; #4 1+x, –1+y, z; #5 1–x, –y, 2–z). (c) The schematic of the (3, 3, 4, 4, 6, 8)-connected 3D framework with $\{4^{11}\cdot6^{12}\cdot8^5\}\{4^2\cdot6\}\{4^3\cdot6^3\}\{4^3\}\{4^4\cdot6^2\}\{4^8\cdot6^6\cdot8\}$ topology.

) of water molecules and carboxylic oxygen atoms (O8, O11 and O4) or the coordinated water molecules (O1W and O2W) and the lattice water molecules (O4W) with the O(1W)–H(1WA)···O(4W), O(2W)–H(2WB)···O(8), O(3W)–H(3WB)···O(8), O(4W)–H(4WB)···O(11) distances of 2.914(15) Å, 2.923(13) Å, 2.981(12) Å and 2.864(15) Å respectively (Table S4).

In the 3D structure, Ni1 ion is connected by four μ_8-bridging **L** ligands and two hydroxyl oxygen atoms, which is generalized as a 6-connected node. Both Ni2 and Ni3 ions linking two μ_8-bridging **L** ligands and two hydroxyl oxygen atoms are regarded as 4-connected nodes. The hydroxyl oxygen atom is bridged to three six-coordinated Ni^{II} ions, which is treated as a 3-connected node. The organic ligand **L** as a 8-connected node is lighted by eight six-coordinated Ni^{II} ions. Finally, the whole framework is symbolized as 6-nodal (3, 3, 4, 4, 6, 8)-connected net with the Schläfli symbol of $\{4^{11}\cdot6^{12}\cdot8^5\}\{4^2\cdot6\}\{4^3\cdot6^3\}\{4^3\}\{4^4\cdot6^2\}\{4^8\cdot6^6\cdot8\}$ (Fig. 4c).

$\{[(CH_3)_2NH_2]_2[Zn(\mathbf{L})]\cdot2DMF\}_n$ (3)

When the Mn^{II} and Ni^{II} were instead of the d^{10} metal Zn^{II}, complex **3** features a 3D framework with pore structures. Different from the above complexes, complex **3** belongs to the monoclinic

system with C2/c space group. Zn1 lies on a twofold axis and that the asymmetric unit has a half **L** ligand lying about an inversion centre, and there is also one DMF molecule and one $(CH_3)_2NH_2^+$ cation, both in general positions. The formation of $(CH_3)_2NH_2^+$ may be due to two reasons. On one hand, it originates from hydrolysis or decarbonylation of DMF molecules. On the other hand, it may be the impurity from DMF [13]. The Zn^{II} ion is encircled by four oxygen atoms (O1, O1#1, O3#2 and O3#3) from four separated **L** ligands, locating in the slightly distorted $\{ZnO_4\}$ tetrahedral style with the Zn–O distances of 1.950(3)–2.005(2) Å (Fig. 5). The completely deprotonated **L** ligand only takes on the monodentate coordination mode with the dihedral angle of 39.49º between the bilaterally parallel phenyl rings and the central phenyl ring (Table 2). The carboxylic oxygen atoms (O3#2 and O3#3) from bilateral phenyl rings and carboxylic oxygen atoms (O1 and O1#1) from the central phenyl ring connect the metal Zn^{II} ions to form different 1D chain, respectively, displaying two kinds of different shapes (wave-like and "H"-like) 1D chains (Fig. 6a). In the wave-like chain, the adjacent **L** ligands are not located in the same plane, including the twist angle of 79.09º between the central phenyl rings from the adjacent **L** ligands. In the "H"-like chain, the distance of the adjacent **L** ligands is about 9.837 Å. Two types of 1D chains link each other to generate the final 3D framework. $(CH_3)_2NH_2^+$ as the counterion play a part in balancing the charges, filling in the framework (Fig. S5). There are about 55% voids in this architecture when the counterions $(CH_3)_2NH_2^+$ and solvent DMF molecules are removed (Fig. S6). Moreover, there are N–H···O hydrogen bonding interactions between the nitrogen atoms (N2) of $(CH_3)_2NH_2^+$ cation and carboxylic oxygen atoms (O4) or the oxygen atom (O5) from DMF molecules with the N(2)–H(2A)···O(4) and N(2)–H(2B)···O(5) distances of 2.823(3) Å and 2.841(4) Å, respectively (Table S5).

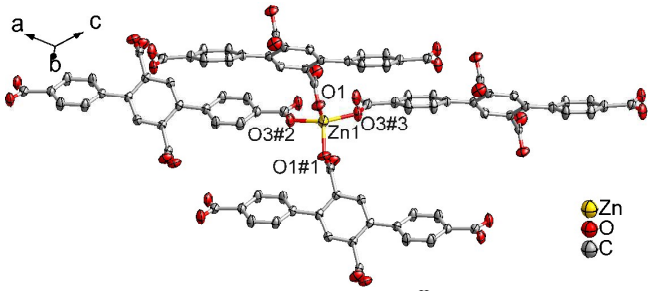

Fig. 5. The coordination environment of the Zn^{II} ion in complex **3** (#1 –x, y, –1/2–z; #2 –x, –y, –z; #3 x, –y, –1/2+z).

From topological viewpoint, each Zn^{II} ion coordinates with four **L** ligands, and one **L** ligand connects four Zn^{II} ions, which are treated as 4-connected nodes. The final framework can be demonstrated as 2-nodal (4, 4)-connected net with the Schläfli symbol of $\{4^2\cdot8^4\}$ (Fig. 6b).

Influence of the different metal ions and the synthesis processes on the structures of complexes 1–3. In our work, we chose [1,1′:4′,1″-terphenyl]-2′,4,4″,5′-tetracarboxylic acid (**H_4L**) ligand and different transition metal ions (Mn^{II}, Ni^{II} and Zn^{II}) as the reactants to synthesize three 3D coordination polymers. In the metal-**H_4L** system, different transition metal ions produce an effect on the coordination modes of **L** ligand. In complex **1**, **H_2L** ligand possessing two protonated

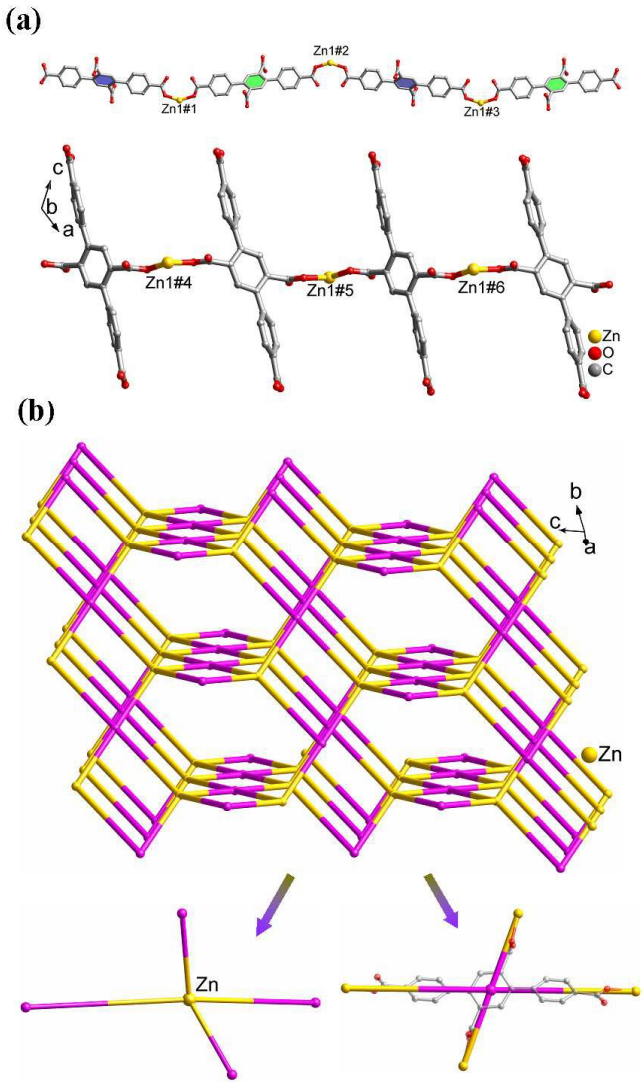

Fig. 6. (a) The wave-like chain and "H"-like chain composed of the carboxyl oxygen atoms from the different positions (#1 –1/2–x, 3/2–y, 1–z; #2 –1+x, y, z; #3 1/2–x, 3/2–y, –z; #4 1–x, 1–y, 1–z; #5 1/2+x, 1/2+y, 1+z; #6 2–x, 1–y, 2–z). (b) The schematic of the (4, 4)-connected 3D framework with $\{4^2\cdot8^4\}$ topology.

carboxy groups is coordinated by six metal Mn^{II} ions with octahedral configuration, and the carboxyl groups from the central phenyl rings and bilaterally phenyl rings are linked by the metal Mn^{II} ions to form 1D chains and 2D layers, respectively, which construct a 6-connected $\{4^{12}\cdot6^3\}$ framework. Compared with complex **1**, although the geometry of Ni^{II} ions from complex **2** is the same as that of Mn^{II} ions, the coordination environments of three crystallographically independent Ni^{II} ions are different from that of Mn^{II} ion. All the carboxylic oxygen atoms from **L** ligand of complex **2** connect with the metal Ni^{II} ions to form a complicated 3D $\{4^{11}\cdot6^{12}\cdot8^5\}\{4^2\cdot6\}\{4^3\cdot6^3\}\{4^3\}\{4^4\cdot6^2\}\{4^8\cdot6^6\cdot8\}$ framework containing two kinds of 1D metal-carboxyl groups chains. Different from the above complexes, metal Zn^{II} ion and **L** ligand from complex **3** are both 4-connected nodes, which lead to the formation of the large pore without $(CH_3)_2NH_2^+$ and DMF guest molecules. This exploration displays that the selection of the transition metal ions plays an important role in the coordination modes of **L** ligand, which further affect the formation of the final

architectures.

On the other hand, the differences of the synthesis processes may lead to the diversities of the 3D frameworks. For complex **1**, metal chloride as the reactant reacts with the **H_4L** ligands under the common hydrothermal condition, obtaining a complex presenting 6-connected $\{4^{12}\cdot6^3\}$ framework. Different from complex **1**, metal salt of complexes **2**–**3** is metal nitrate, and complexes **2**–**3** have been adjusted by HCl aqueous solution, which results in the formation of complicated complex **2** and complex **3** possessing pores. For complex **3**, the addition of DMF solvent is propitious to the formation of large pore. Thus it can be seen that the synthesis processes have an important influence on structures of the title complexes.

Fluorescent properties

The solid state fluorescence spectra for complexes **1–3** and the free **H_4L** ligand have been researched at the room temperature (Fig. 7). In the process of measurement, all the test conditions are identical. The excitation peaks of the title complexes and **H_4L** ligand are at 280 nm, and both the excitation slit and emission slit are 1.0 nm. The **H_4L** ligand exhibits the emission spectrum with maxima at 413 nm. For the title complexes, complexes **1–2** have no fluorescent response, while complex **3** possesses the obvious emission broad peak with maxima at 368 nm, displaying the distinct blue shift compared to the free **H_4L** ligand, which may be ascribed to the metal-to-ligand charge transfer, intraligand and ligand-to-metal charge transfer [14]. In addition, the fluorescent intensity of complex **3** is greatly higher than those of complexes **1–2**, which may be due to the existence of core-like d-orbitals and the absence of d–d transition from the d^{10} Zn^{II} [14b].

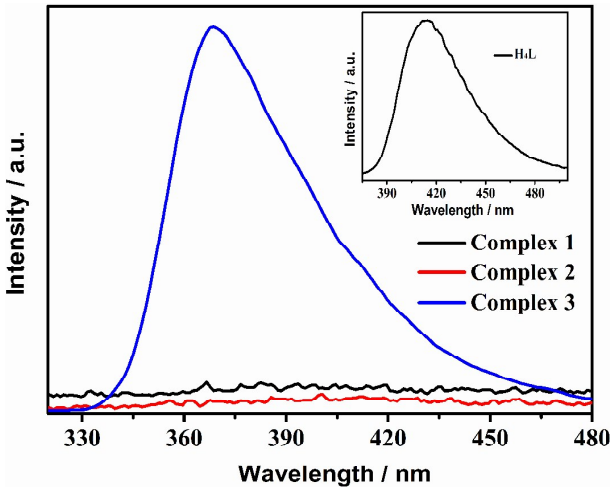

Fig. 7. The solid-state fluorescence spectra of complexes **1**–**3** at room temperature. The inset shows the solid-state fluorescence spectrum of the free ligand **H_4L** at room temperature.

Electrochemical behavior of 1–2–CPE.

Because Mn^{II} and Ni^{II} complexes can undergo reversible redox processes, the electrochemical behaviors of complexes **1–2** bulk-modified carbon paste electrode (**1**–CPE and **2**–CPE) are investigated in 0.01 M H_2SO_4 + 0.5 M Na_2SO_4 aqueous solution. Fig. S10 and Fig. 8a display the cyclic voltammograms of **1–2**–CPEs at different scan rates in the potential range 0 to 800 mV for **1**, 100 to 800 mV for **2**. There are a couple of reversible redox peaks (I–I′) at the modified CPEs, which may be assigned to the redox of Mn^{III}/Mn^{II} or Ni^{III}/Ni^{II} [15], and the mean peak potential $[E_{1/2} = (E_{pa} + E_{pc})/2]$ is 422 mV for **1** and 415 mV for **2** with the scan rate of 100 mVs^{-1} (Fig. S11–S12). When the scan rates increase from 25 to 500 mVs^{-1}, the peak potentials gradually shift: the cathodic peak potentials shifted to negative direction and the corresponding anodic peak potentials shifted to positive direction. In the inserts of Fig. S10 and Fig. 8a, the redox peak currents are proportional to scan rates up to 500 mVs^{-1}, revealing that the redox of **1–2–**CPE is the surface-confined process.

Fig. 8b presents electrocatalytic activity of **2–**CPE for reduction of nitrite. When nitrite with different concentrations is added into the 0.01 M H_2SO_4 + 0.5 M Na_2SO_4 aqueous solution, the reduction peak currents gradually increase, and the corresponding oxidation peak currents decrease, indicating that **2–**CPE has good electrocatalytic activity to the reduction of nitrite.

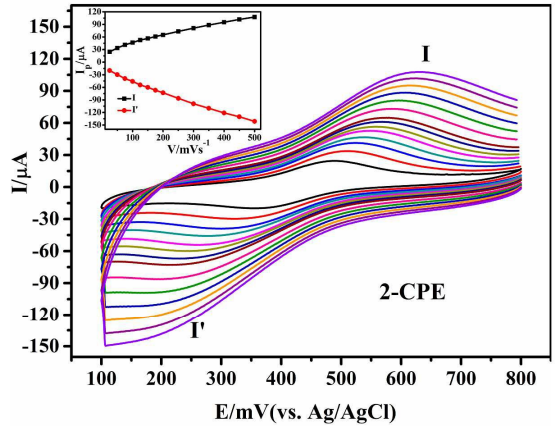

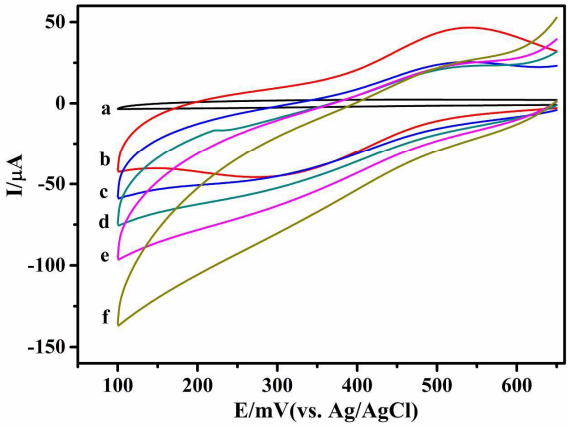

Fig. 8. (a) Cyclic voltammograms of the 2–CPE in 0.01 M H2SO4 + 0.5 M Na2SO4 aqueous solution at different scan rates (from inner to outer: 25, 50, 75, 100, 125, 150, 175, 200, 250, 300, 350, 400, 450, 500 mV·s-1). The inset shows the plots of the anodic and cathodic peak currents against scan rates. (b) Cyclic voltammograms of the bare CPE in 0.01 M H2SO4 + 0.5 M Na2SO4 solution (a), 2-CPE in 0.01 M H2SO4 + 0.5 M Na2SO4 solution containing 0.0, 1.0, 2.0, 3.0 and 4.0 mmol NaNO2 (b∼f). Scan rate: 100 mVs-1.

Photocatalytic activities.

Photocatalysts have been a focus on purifying water and air by decomposing organic dyes. To study the photocatalytic activities of complexes **1–3**, methylene blue (MB) is selected as model of dye pollutant, and in the course of degradation, MB can be broken

down into non-polluting molecules under visible light irradiation. For the organic ligand **H_4L**, it is induced to produce oxygen-metal charge transfer, which enhances electrons from the highest occupied molecular orbital (HOMO) to the lowest unoccupied molecular orbital (LUMO). The electron was caught from water molecules because HOMO requires one electron to return the stable state, which was oxygenated to generate the ·OH radicals [16a]. Then MB can be effectively disintegrated by ·OH active species, finishing the photocatalytic process [16a].

The processes of photocatalytic experiments are as follows: 100 mg crystals were added in 200 mL MB aqueous solution (10.0 mg /L), stirred in the dark for 30 min magnetically to ensure the adsorption/desorption equilibrium. Then the mixture was irradiated through an xenon lamp and kept stirring. Suspension (3 mL) was taken out from the reactor every 20 min and handled in the method of centrifugal separation. The clear solution was analyzed by UV-visible spectroscopy. Moreover, the MB without any photocatalyst has also been carried out under the same conditions.

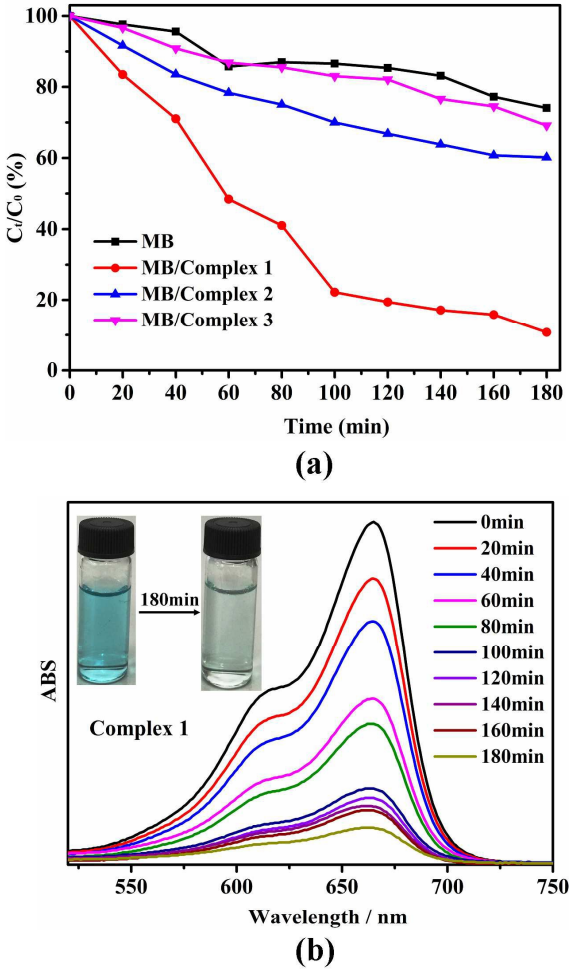

Fig. 9. (a) Photocatalytic decomposition rates of MB solution under the visible light irradiation with the use of the complexes 1–3 and no crystal in the same conditions. (b) Absorption spectra of the MB solution during the decomposition reaction under the visible light irradiation with the presence of complex 1. The inset shows the color change of the MB solution after the visible light irradiation for complex 1.

The degradation of MB without any catalyst has no significant change in the visible light irradiation (Fig. S13a). While when complexes **1–3** act as the photocatalysts, there are some changes in the degradation of MB. The absorption intensities of MB decreased gradually with the increase of illumination time. The plot of concentrations of MB (C) versus irradiation times (t) is shown in Fig. 9a. The degradations increase from about 25.2% (without any catalyst) to 89.21% for **1**, 39.8% for **2**, 30.8% for **3** after 180 min. The title complexes display the photocatalytic activities in the degradation of MB (Fig. 9a and Fig. S13). After photocatalysis, the MB solution color has great change varying from dark blue to light blue. Moreover, the control experiments of the title reactants ($MnCl_2·4H_2O$, $Ni(NO_3)_2·6H_2O$, $Zn(NO_3)_2·6H_2O$ and **H_4L**) have been examined, and there is no obvious change for the degradation of MB. The result displays that complex **1** possesses good photocatalytic activity (Fig. 9b), which may be the potential photoactive materials.

Fig. S8 reveals that the PXRD peaks after the photocatalytic experiments are almost identical to that of the fresh complexes, which suggests the stabilities of the complexes **1–3**. Three complexes exhibit different catalytic activities because of the selection of organic ligands, coordination conjugation of the metal ions and the differences of the final frameworks.

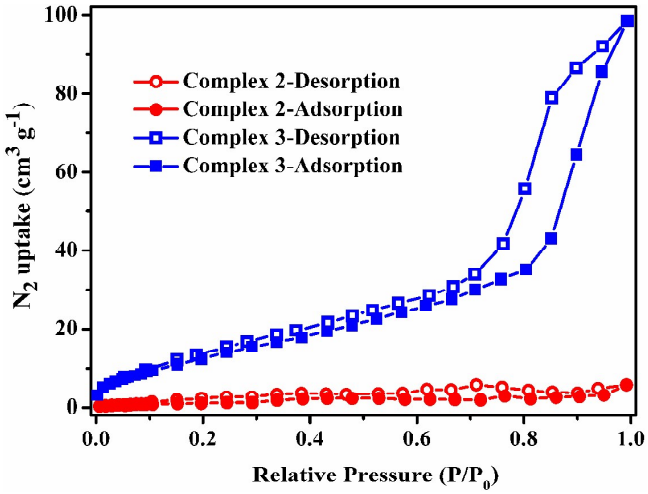

Fig. 10. N_2 adsorption–desorption isotherms for complexes **2**–**3** at 77 K.

Nitrogen adsorption properties.

To explore the nitrogen adsorption properties of complexes **2–3**, the adsorption isotherms were accomplished at 77 K (Fig. 10). The samples were heated at 150 °C for **2** and 200 °C for **3** under the vacuum condition for 10 h in order to remove the guest molecules from the 3D framework. For complex **2**, the nitrogen adsorption isotherm has no obvious rise in the whole process of the nitrogen adsorption. The N_2 uptake value is only 5.7 cm^3g^{-1}, Brunauer-Emmett-Teller (BET) surface area is 4.159 m^3g^{-1} and the pore volume is 0.008 cm^3g^{-1}, which indicates that complex **2** exhibits the non-porosity architecture. Comparatively speaking, complex **3** shows the distinctly rising adsorption isotherm, and it has the N_2 uptake amount of 98.4 cm^3g^{-1}, a BET surface area of 53.028 m^3g^{-1} and a pore volume of 0.138 cm^3g^{-1}. When the relative pressure P/P_0 is in the range of 0.0–0.8, the nitrogen adsorption isotherm displays a slow rise. After $P/P_0 > 0.8$, the amount of nitrogen adsorption increases rapidly, and the final maximum adsorption value is about 98.4 cm^3g^{-1} at $P/P_0 = 0.99$. In the course of desorption, the nitrogen desorption isotherm shows a slow decline relative to the adsorption isotherm in the high relative pressure, and the amount is about 41.9 cm^3g^{-1} at relative pressure

P/P_0 = 0.76, displaying the obvious hysteresis. In the low relative pressure, the hysteresis generally weakens. The above phenomenon illustrates that some N_2 molecules may be adsorbed in the 3D framework in the high relative pressure due to boundedness of the pore sizes from complex **3**. The X-ray powder diffraction pattern after nitrogen adsorption reveals that the framework retain the stability (Fig. S8).

Conclusion

In conclusion, by changing the different metal ions, three new diverse 3D MOFs based on [1,1′:4′,1″-terphenyl]-2′,4,4″,5′-tetracarboxylic acid (**H_4L**) ligands were obtained. The difference of the metal ions and the synthesis processes leads to the distinction of coordinate modes from the **H_4L** ligands, having an influence on the final 3D frameworks. Meanwhile, the title complexes containing different metal ions display different properties. For fluorescent properties, complex **3** possesses the high fluorescent intensity compared with the other complexes. For electrochemical properties, complex **2** has electrocatalytic activity to the reduction of nitrite. In photocatalytic properties, complex **1** exhibiting good catalytic activity for the degradation of MB may be the potential photocatalytic material. In addition, complex **3** has the nitrogen adsorption capacity.

Acknowledgement

This work was supported by the Program for National Nature Science Foundation of China (nos. 21271024 and 20971014) and Foundation the 111 Project (B07012) in China.

Notes and references

1 (a) R. B. Getman, Y. S. Bae, C. E. Wilmer and R. Q. Snurr, *Chem. Rev.*, 2012, **112**, 703; (b) J. R. Li, J. Sculley and H. C. Zhou, *Chem. Rev.*, 2012, **112**, 869; (c) H. Furukawa, N. Ko, Y. B. Go, N. Aratani, S. B. Choi, E. Choi, A. O. Yazaydin, R. Q. Snurr, M. O'Keeffe, J. Kim and O. M. Yaghi, *Science*, 2010, **329**, 424; (d) Z. C. Hu, B. J. Deibert and J. Li, *Chem. Soc. Rev.*, 2014, **43**, 5815; (e) C. B. He, K. D. Lu and W. B. Lin, *J. Am. Chem. Soc.*, 2014, **136**, 12253.

2 (a) L. Ma, C. Abney and W. Lin, *Chem. Soc. Rev.*, 2009, **38**, 1248; (b) J. P. Zhang, Y. B. Zhang, J. B. Lin and X. M. Chen, *Chem. Rev.*, 2012, **112**, 1001; (c) M. Hirscher, *Angew. Chem. Int. Ed.*, 2011, **50**, 581; (d) X. Zhao, X. H. Bu, Q. G. Zhai, H. Tran and P. Y. Feng, *J. Am. Chem. Soc.*, 2015, **137**, 1396; (e) H. C. Zhou and S. Kitagawa, *Chem. Soc. Rev.*, 2014, **43**, 5415; (f) W. Y. Gao, Y. Chen, Y. H. Niu, K. Williams, L. Cash, P. J. Perez, L. Wojtas, J. F. Cai, Y. S. Chen and S. Q. Ma, *Angew. Chem. Int. Ed.*, 2014, **53**, 2615.

3 (a) A. Fujishima, X. Zhang and D. A. Tryk, *Surf. Sci. Rep.*, 2008, **63**, 515; (b) A. Kar, Y. R. Smith and V. Subramanian, *Environ. Sci. Technol.*, 2009, **43**, 3260; (c) H. X. Li, X. Y. Zhang, Y. N. Huo and J. Zhu, *Environ. Sci. Technol.*, 2007, **41**, 4410; (d) Z. L. Liao, G. D. Li, M. H. Bi and J. S. Chen, *Inorg. Chem.*, 2008, **47**, 11.

4 (a) Y. Q. Chen, S. J. Liu, Y. W. Li, G. R. Li, K. H. He, Y. K. Qu, T. L. Hu and X. H. Bu, *Cryst. Growth Des.*, 2012, **12**, 5426; (b) L. L. Wen, J. B. Zhao, K. L. Lv, Y. H. Wu, K. J. Deng, X. K. Leng and D. F. Li, *Cryst. Growth Des.*, 2012, **12**, 1603; (c) J. Guo, J. Yang, Y. Y. Liu and J. F. Ma, *CrystEngComm*, 2012, **14**, 6609; (d) Y. Q. Chen, G. R. Li, Y. K. Qu, Y. H. Zhang, K. H. He, Q. Gao and X. H. Bu, *Cryst. Growth Des.*, **2013**, 13, 901.

5 (a) X. L. Wang, J. J. Huang, L. L. Liu, G. C. Liu, H. Y. Lin, J. W. Zhang, N. L. Chen and Y. Qu, *CrystEngComm*, 2013, **15**, 1960; (b) X. L. Wang, J. Luan, F. F. Sui, H. Y. Lin, G. C. Liu and C. Xu, *Cryst. Growth Des.*, 2013, **13**, 3561; (c) X. L. Wang, F. F. Sui, H. Y. Lin, J. W. Zhang and G. C. Liu, *Cryst. Growth Des.*, 2014, **14**, 3438; (d) X. L. Wang, X. T. Sha, G. C. Liu, N. L. Chen and Y. Tian, *CrystEngComm*, 2015, **17**, 7290; (e) M. Li, S. Zhao, Y. F. Peng, B. L. Li and H. Y. Lia, *Dalton Trans.*, 2013, **42**, 9771; (f) H. H. Wang, J. Yang, Y. Y. Liu, S. Y. Song and J. F. Ma, *Cryst. Growth Des.*, 2015, **15**, 4986.

6 (a) M. Li, S. Zhao, Y. F. Peng, B. L. Li and H. Y. Li , *Dalton Trans.*, 2013, **42**, 9771; (b) L. Liu, J. Ding, C. Huang, M. Li, H. W. Hou and Y. T. Fan, *Cryst. Growth Des.*, 2014, **14**, 3035.

7 (a) J. S. Qin, S. R. Zhang, D. Y. Du, P. Shen, S. J. Bao, Y. Q. Lan and Z. M. Su, *Chem. Eur. J.*, 2014, **20**, 5625; (b) L. Sun, C. H. Hendon, M. A. Minier, A. Walsh and M. Dinca, *J. Am. Chem. Soc.*, 2015, **137**, 6164; (c) M. J. Katz, J. E. Mondloch, R. K. Totten, J. K. Park, S. T. Nguyen, O. K. Farha and J. T. Hupp, *Angew. Chem., Int. Ed.*, 2014, **53**, 497.

8 (a) A. Y. Robin and K. M. Fromm, *Coord. Chem. Rev.*, 2006, **250**, 2127; (b) Y. Yu, J. P. Ma, C. W. Zhao, Jing Yang, X. M. Zhang, Q. K. Liu and Y. B. Dong, *Inorg. Chem.*, 2015, **54**, 11590; (c) T. Gong, X. Yang, Q. Sui, Y. Qi, F. G. Xi and E. Q. Gao, *Inorg. Chem.*, 2016, **55**, 96; (d) Z. C. Hu, W. P. Lustig, J. M. Zhang, C. Zheng, H. Wang, S. J. Teat, Q. H. Gong, N. D. Rudd and J. Li, *J. Am. Chem. Soc.*, 2015, **137**, 16209.

9 (a) D. S. Chen, H. Z. Xing, Z. M. Su and C. G. Wang, *Chem. Commun.*, 2016, DOI: 10.1039/C5CC09065B; (b) T. P. Hu, B. H. Zheng, X. Q. Wang and X. N. Hao, *CrystEngComm*, 2015, **17**, 9348; (c) B. K. Tripuramallu, H. M. Titi, S. Roy, R. Verma and I. Goldberg, *CrystEngComm*, 2016, DOI: 10.1039/C5CE02048D; (d) T. T. Fan, J. J. Li, X. L. Qu, H. L. Han and X. Li, *CrystEngComm*, 2015, **17**, 9443.

10 (a) Y. X. Shi, F. L. Hu, W. H. Zhang and J. P. Lang, *CrystEngComm*, 2015, **17**, 9404; (b) F. R. Dai, Y. P. Qiao and Z. Q. Wang, *Inorg. Chem. Front.*, 2016, DOI: 10.1039/C5QI00212E; (c) S. Z. Wang, W. Morris, Y. Y. Liu, C. M. McGuirk, Y. Zhou, J. T. Hupp, O. K. Farha and C. A. Mirkin, *Angew. Chem. Int. Ed.*, 2015, **54**, 14738; (d) Y. P. He, Y. X. Tan and J. Zhang, *Inorg. Chem.*, 2012, **51**, 11232; (e) H. Chevreau, T. Devic, F. Salles, G. Maurin, N. Stock and C. Serre, *Angew. Chem. Int. Ed.*, 2013, **52**, 5056; (f) W. G. Lu, D. Q. Yuan, T. A. Makala, Z. W. Weia, J. R. Lia and H. C. Zhou, *Dalton Trans.*, 2013, **42**, 1708.

11 (a) F. Gandara, H. Furukawa, S. Lee, and O. M. Yaghi, *J. Am. Chem. Soc.*, 2014, **136**, 5271; (b) L. L. Lv, J. Yang, H. M. Zhang, Y. Y. Liu and J. F. Ma, *Inorg. Chem.*, 2015, **54**, 1744.

12 G. M. Sheldrick, *Acta Crystallogr., Sect. A: Found. Crystallogr.*, 2008, **64**, 112; (b) L. J. Bourhis, O. V. Dolomanov, R. J. Gildea, J. A. K. Howard and H. Puschmann, *Acta Cryst.* 2015, **A71**, 59; (c) O. V. Dolomanov, L. J. Bourhis, R. J. Gildea, J. A. K. Howard and H. Puschmann, *J. Appl. Cryst.* 2009, **42**, 339.

13 A. D. Burrows, K. Cassar, T. Düren, R. M. W. Friend, M. F. Mahon, S. P. Rigby and T. L. Savaresea, *Dalton Trans.*, 2008, **18**, 2465.

14 (a) Y. J. Cui, Y. F. Yue, G. D. Qian and B. L. Chen, *Chem. Rev.*, 2012, **112**, 1126; (b) H. Y. Li, L. H. Cao, Y. L. Wei, H. Xu and S. Q. Zang, *CrystEngComm*, 2015, **17**, 6297.

15 (a) T. V. Mitkina, N. F. Zakharchuk, D. Y. Naumov, O. A. Gerasko, D. Fenske and V. P. Fedin, *Inorg. Chem.*, 2008, **47**, 6748; (b) J. Britten, N. G. R. Hearns, K. E. Preuss, J. F. Richardson, and S Bin-Salamon, *Inorg. Chem.*, 2007, **46**, 3934.

16 (a) H. X. Yang, T. F. Liu, M. N. Cao, H. F. Li, S. Y. Gao and R. Cao, *Chem. Commun.*, 2010, **46**, 2429; (b) J. X. Meng, Y. Lu, Y. G. Li, H. Fu and E. B. Wang, *CrystEngComm*, 2011, **13**, 2479; (c) J. Guo, J. Yang, Y. Y. Liu and J. F. Ma, *CrystEngComm*, 2012, **14**, 6609.

The electrochemical properties, nitrogen adsorption and photocatalytic activities of three 3D metal–organic frameworks bearing the rigid terphenyl tetracarboxylates ligands

Bao Mu, Chang-xia Li, Ming Song, Yan-li Ren, Ru-dan Huang*

Key Laboratory of Cluster Science of Ministry of Education, School of Chemistry, Beijing Institute of Technology, Beijing, 100081, P. R. China

Three new 3D metal–organic frameworks (MOFs) derived from the rigid terphenyl tetracarboxylates ligands with different transition metal ions have been successfully prepared. The effect of three kinds of metal ions on the architectures of complexes **1**–**3** have been investigated in detail. In addition, the title complexes exhibit different properties. The fluorescence and photocatalytic properties of complexes **1**–**3**, the electrochemical behaviors of complex **2** and the nitrogen adsorption property of complex **3** have also been studied.

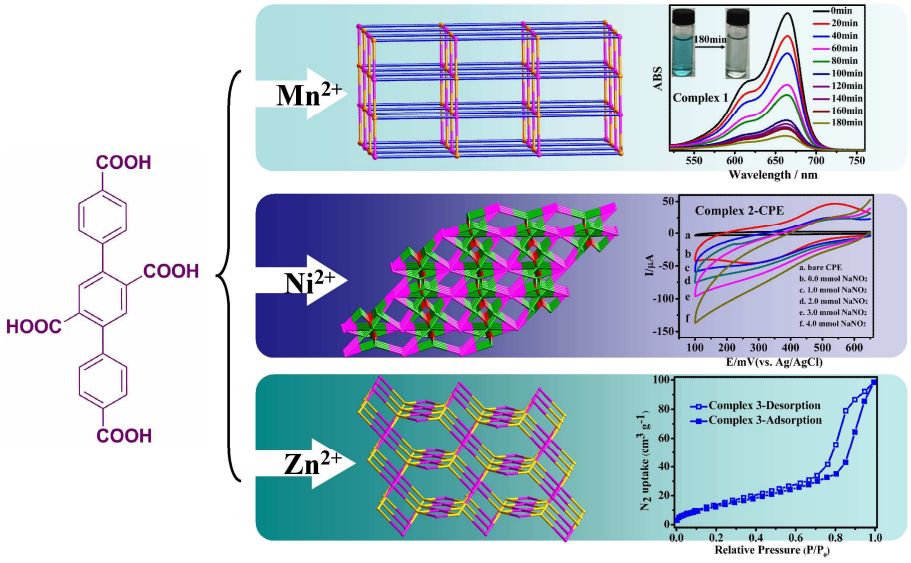

* Corresponding author. *E-mail address:* huangrd@bit.edu.cn (R. D. Huang).